Electrochimica Acta 388 (2021) 138522

Contents lists available at ScienceDirect

Electrochimica Acta

journal homepage: www.elsevier.com/locate/electacta

An additive-free silicon anode in nanotube morphology as a model lithium ion battery material

Ying Zhuo[a], Hong Sun[a], Md. Helal Uddin[a], Maïssa K.S. Barr[a], Dorothea Wisser[b], Philip Roßmann[b], Julian D. Esper[c], Sarah Tymek[a], Dirk Döhler[a], Wolfgang Peukert[c], Martin Hartmann[b], Julien Bachmann[a,d,*]

[a] Department of Chemistry and Pharmacy, Chemistry of Thin Film Materials, Friedrich-Alexander University of Erlangen-Nürnberg, IZNF / Cauerstr. 3, Erlangen 91058, Germany
[b] Department of Chemical and Biological Engineering, Erlangen Center for Interface Research and Catalysis, Friedrich-Alexander University of Erlangen-Nürnberg, Egerlandstr. 3, Erlangen 91058, Germany
[c] Department of Chemical and Biological Engineering, Friedrich-Alexander University of Erlangen-Nürnberg, Institute of Particle Technology (LFG), Cauerstr. 4, Erlangen 91058, Germany
[d] Saint Petersburg State University, Institute of Chemistry, Universitetskii pr. 26, Saint Petersburg 198504, Russian Federation

ARTICLE INFO

Article history:
Received 2 November 2020
Revised 14 April 2021
Accepted 27 April 2021
Available online 7 May 2021

Keywords:
Si nanotube
Atomic layer deposition
Aluminothermic reduction
Anode material
Lithium ion battery

ABSTRACT

Ordered arrays of parallel, cylindrical silicon nanotubes are obtained by aluminothermic reduction of SiO_2 nanotubes generated by atomic layer deposition (ALD) on nanoporous aluminum oxide templates. The reduction to amorphous Si (a-Si) is characterized by a combination of X-ray diffraction (XRD), solid-state cross-polarization magic-angle spinning nuclear magnetic resonance (^{29}Si CP-MAS NMR), ultraviolet-visible spectroscopy, attenuated total reflectance infrared spectroscopy (ATR-IR), and X-ray photoelectron spectroscopy (XPS). These a-Si nanotube arrays are electrochemically active in a lithium-ion battery environment when prepared on Cu current collectors without any additives. The absence of the traditional additive carbon black, which is an electrochemically inert conductor, increases the proportion of capacity associated with faradaic reactions (Li incorporation) with respect to the capacitive component. Electrochemical impedance spectroscopy (EIS) and charge-discharge tests demonstrate that the nanotube morphology yields an improved tolerance to fast cycling.

1. Introduction

A widespread use of sustainable and renewable energy sources is needed in order to replace fossil fuel resources and reduce greenhouse gas emissions. However, most renewable energy sources, such as wind [1–3] and solar energy [4,5,–6] are intermittent and require energy storage systems for grid management and portable applications. Among the various storage technologies, the lithium-ion battery is the prime choice for portable devices and electric vehicles [7]. In presently commercial Li-ion batteries, the graphite anode (the negative electrode) limits performance due to its low specific capacity of 372 mAh g^{-1} [8,9]. The most prominent alternative to graphite, which bases on an intercalation mechanism with finite capacity [10,11], is provided by silicon and other group IV elements, which can alloy in Li to higher stoichiometries [12–14]. In particular, Si presents some particularly attractive properties: (1) The stoichiometry $Li_{4.4}Si$ [10,15,16] yields an extremely large theoretical gravimetric specific capacity of 4200 mAh g^{-1} [13,16,17] (volumetric 9786 mAh cm^{-3}) [10,14]; (2) Its low delithiation voltage (0.2 V to 0.6 V vs. Li/Li^{+}) [12,15], delivers high working voltages in full cells hence increases the energy density [10]. (3) Si is the second most abundant element in the earth's crust and environmentally benign [9,10,14,15,17]. Despite these advantages, the enormous volume expansion (~ 300%) associated with its lithiation [9,12,16,18] inflicts such stress and strain on the material that the anode typically cracks, breaks and even disintegrates upon cycling, in addition to featuring an unstable solid electrolyte interface (SEI) layer [9]. These phenomena cause rapid failure of the batteries, especially under

* Corresponding author at: Department of Chemistry and Pharmacy, Chemistry of Thin Film Materials, Friedrich-Alexander University of Erlangen-Nürnberg, IZNF / Cauerstr. 3, Erlangen 91058, Germany.
E-mail address: julien.bachmann@fau.de (J. Bachmann).

https://doi.org/10.1016/j.electacta.2021.138522

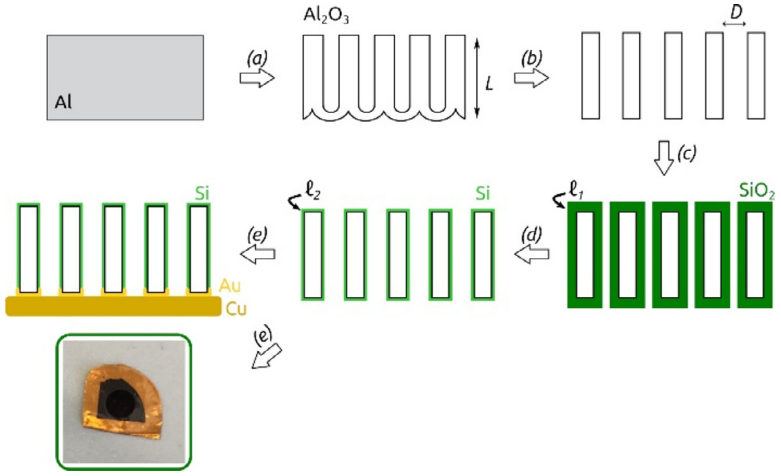

Fig. 1. Schematic presentation of the preparative procedures towards Si nanotubes. *(a)* Two-step anodization to build well ordered Al_2O_3 nanopores with subsequent wet chemical removal of metallic Al. The length L of the AAO membranes is defined by this step. *(b)* Wet chemical Al_2O_3 barrier layer etching and pore widening (defining the outer tube diameter D) in H_3PO_4 solution. *(c)* ALD of SiO_2, precisely defining the tube wall thickness ℓ_1. *(d)* Laser-cut of the sample before reduction of SiO_2 to Si and by-product removal. ℓ_2 is the wall thickness of Si nanotubes after reduction. *(e)* Sputter-coating of Au on one side of the sample and gluing with conductive Cu adhesive tape onto Cu foil as a current collector. The photograph of one real sample is displayed, allowing one to discern the 4 mm diameter mask used to define the sample area.

fast cycling conditions. Additional limitations include the low electrical conductivity of Si (~ 10^{-3} S cm^{-1}) [13,19] and slow Li-ion diffusion velocity (diffusion coefficient of 10^{-13} to 10^{-14} cm^2 s^{-1}) [10,12,13,19].

Si as an anode material can benefit of controlling its morphology on the sub-micrometer scale in two ways. Firstly, a controlled porosity can significantly alleviate the stress and strain on the anode [20] and thus maintain a longer lifetime. Secondly, the paths of electrons from the electrode and Li ions from the electrolyte can be straightened and shortened, thereby giving rise to a better rate performance of Si anodes [13]. Therefore, tremendous efforts have been devoted to the design and development of nanostructured Si anodes, such as 0D nanoparticles [21–24], 1D nanowires [25,26], nanorods [27] and nanotubes [28], 2D thin films and nanosheets [29] and 3D porous nanostructures [30–32].

We note that silicon in negative lithium ion battery electrodes should be amorphous for success – this is a fact that has been clearly established by a number of primary studies [26,33–35], and is stated unambiguously in leading reviews in the field [13,36,37]. When crystalline Si is charged, Li ion diffusion and incorporation is hindered. Therefore, the first charge occurs with significant overpotential and with a larger volume expansion than if amorphous Si is used. Subsequent discharge generates Si in its amorphous form (a-Si), and the electrode then behaves accordingly.

Therefore, in this work, we propose a cylindrical nanotube morphology for a-Si as a Li-ion battery anode. Amorphous Si is generated from SiO_2 nanotubes by aluminothermic reduction. The amorphous SiO_2 nanotubes are fabricated via atomic layer deposition (ALD) on 'anodic' aluminum oxide (AAO), which serves as a template. This structure has been exploited successfully for SnO_2-based anodes [38], the geometric parameters of which (length L, outer pore diameter D, and wall thickness of ℓ_1 of the nanotubes, Fig. 1) can be precisely tuned. Here, we use the parameters found to be optimal in our previous work, namely $L = 30$ μm $D = 380$ nm. The tube wall thickness is adjusted by the deposition method. 500 cycles of SiO_2 ALD yield 40 nm of SiO_2, which then shrink by approximately a factor three upon reduction to a-Si [39]. This reduction reaction is performed by aluminothermic means, which is experimentally much simpler to carry out with large samples than the lithium vapor procedure used earlier. Electrochemical characterization of this additive-free Si nanotube system points out the differences between it and classical slurry-derived samples.

2. Experimental section

2.1. Materials

Ethanol, perchloric acid (70%), phosphoric acid, chromium(VI) oxide, copper(II) chloride dihydrate, hydrochloric acid (37%), nitric acid (65%), 3-aminopropyltriethoxysilane (APTES), diethyl ether, aluminum, aluminum chloride ($AlCl_3$), metallic Li, 1.0 M lithium hexafluorophosphate ($LiPF_6$) in 50:50 (v/v) ethylene carbonate (EC) and diethyl carbonate (DEC) solution and Cu foil were purchased from abcr, VWR or Sigma Aldrich and used as received. Aluminum plates (0.5 mm thick) were provided by Smart Membranes. Water was purified in a Millipore Direct-Q System. Au target for sputtering was supplied by Stanford Advanced Materials. Silicon wafers coated with an oxide layer were from Silicon Materials Inc. CR2032 cases, stainless steel spacers and springs were purchased from MTI Corporation. Celgard 2325 separators were from EL-Cell GmbH.

2.2. Preparation of 'anodic' aluminum oxide (AAO) template

A two-step anodization (Fig. 1**a**) was performed to fabricate 'anodic' aluminum oxide (AAO) membranes. Before the anodization, aluminum plates (2 × 2 cm^2) were electropolished in a cold 1:3 (v/v) mixture of concentrated $HClO_4$ and ethanol with stirring at 20 V for about 5 min to gain mirror-like smooth surfaces. Subsequently, these aluminum plates were anodized in 0.5 wt% H_3PO_4 solution for 1 h aunder+ 195 V at 0 °C at first, then anodization was pursued in 1 wt% H_3PO_4 for another 23 h. During anodization, a two-electrode system was used. Aluminum plates were sealed between a PVC beaker with O-ring on top and a Cu plate underneath. The aluminum plates together with the Cu plate are connected to the anode of the power supply while the PVC beaker containing the H_3PO_4 solution (the electrolyte) was covered by a cap providing the counter-electrode (silver wire mesh) and a mechanical stirrer. After the first anodization, chromic acid solution (0.18 M CrO_3 in 6 wt% H_3PO_4) was used to remove the irregularly grown aluminum oxide nanopores for 24 h at 45 °C. The second anodization was executed under +195 V and at 0 °C, first for 1 h in 0.5 wt% H_3PO_4 and subsequently for 9 h in 1 wt% H_3PO_4. The aluminum substrate was later removed with 0.7 M $CuCl_2$ in 10 % HCl. 10 wt% H_3PO_4 solution was used to remove the barrier layer of the

AAO membrane (35 min from the back side) and pore widening at 45 °C (full immersion in H_3PO_4 for another 35 min) (Fig. 1**b**).

2.3. Preparation of Si nanotubes

Deposition of SiO_2 via atomic layer deposition (ALD). SiO_2 nanotubes were deposited by ALD (Fig. 1**c**), which is accomplished in a commercial Gemstar–6 XT ALD reactor from Arradiance. The ALD reaction was performed at 170 °C under pressure around 800 mTorr with 3-aminopropyltriethoxysilane (APTES) as the metal precursor while water and ozone were used as oxygen source (co-reactants). APTES was heated up to 70 °C. Ozone was generated in situ by an ozone generator BMT 803N with 50% power. The gaseous precursors were transported towards the ALD reactor by 100 sccm N_2 flow, which acted as carrier gas. The pulse sequences for APTES, H_2O and O_3 were (0.7 s | 60 s | 120 s), (0.5 s | 50 s | 90 s) and (0.2 s | 50 s | 90 s), respectively. The growth rate of SiO_2 ALD is 0.8 Å/cycle. Si (100) wafers with native oxide layer (~ 200 nm) were used as the indicator to monitor the thin film growth by spectroscopic ellipsometry.

Aluminothermic reduction of SiO_2. The samples of as-deposited SiO_2 on AAO template were transparent and slightly milky (**Fig. S1a**). The samples were laser-cut out of their Al frames with a GCC LaserPro Spirit LS laser before performing the reduction. Si nanotubes were obtained by an aluminothermic reduction reaction with a mixture of Al and $AlCl_3$ tested in various mass ratios. The reduction was carried out by assembling the sample and the reductants in a tightly sealed autoclave, model 4652 from Parr Instrument Company with a temperature controller LTR 3500 with cTron from Juchheim, which was filled with Ar. The sample and the Al/$AlCl_3$ mixture were placed on one stainless steel sample holder separately. The reduction was conducted in Ar atmosphere at 400 °C for 10 h after a heating ramp of 76 °C/h. Subsequently, the samples, which had turned black (**Fig. S1b**), were rinsed with diethyl ether immediately after disassembling the autoclave, in order to remove unreacted $AlCl_3$. The samples were then heated to 50 °C for a half-hour before being immersed in 10 wt% H_3PO_4 at 50 °C for 3 min to remove all other reaction by-products (Fig. 1**d**).

2.4. Characterization

X-ray diffraction (XRD) with Cu Kα_1 radiation (λ = 1.54056 Å) on a Bruker D8 Advance diffractometer equipped with a LynxEye XE-T detector was used to investigate the crystal structure of the samples. The measurements were performed in the regular Bragg-Brentano geometry for porous samples. Ultraviolet-visible absorption spectroscopy were performed with OceanOptics spectrometer DH-2000-BAL. Jasco 4100 FT-IR spectrometer from JASCO Deutschland GmbH was used to record fourier transform Infrared (FT-IR) spectra using a DLaTGS detector with 4 cm^{-1} resolution. Solid-state NMR spectra under magic angle spinning (MAS) were measured on an Agilent 500 WB instrument (11.7 T) with resonance frequency of 99.31 MHz for ^{29}Si nuclei. All spectra were referenced indirectly to sodium trimethylsilylpropanesulfonate (DSS). ^{29}Si cross-polarization (CP) spectra were recorded at a MAS rate of 15 kHz, accumulating up to 4000 scans with inter-scan delay of 2.5 s. After a 2.6 s $\pi/2$ pulse on protons, the RF of protons was ramped linearly from 72 to 91 kHz (80 to 100%) during 5 ms, while keeping the ^{29}Si RF field at 77 kHz. 100 kHz ^{1}H spinal–64 decoupling was applied during acquisition. Scanning electron microscopy (SEM) and energy-dispersive X-ray spectroscopy (EDX) were performed to the samples with an Jeol JSM 6400 upgraded with a LaB_6 cathode and SDD X-ray detector. Raman spectroscopy was carried out for the samples with a WITec alpha-R Confocal Raman Microscope in backscattering geometry with 532 nm excitation wavelength. X-ray photoelectron spectroscopy (XPS) was carried out with monochromatized Al Kα on a PHI Quantera II, Japan.

2.5. Si nanotube electrode preparation

The Si nanotube samples obtained after reduction were dried in the oven, a layer of gold as the contact layer (approximately 100 nm) was then sputtered onto one side of the samples in a Torr CRC 622 sputter coater. Samples were finally glued onto a Cu foil as the current collector with a double-sided adhesive and conducting Cu adhesive tape (Fig. 1**e**).

2.6. Electrochemical measurements

The as-prepared Si nanotubes with AAO template samples were masked by polyamide tape (Kapton®) with a defined circular area of 4 mm diameter for electrochemical measurements. The polyamide tape (Kapton®) is chemically resistant and electrically insulating. For building an electrochemical cell, the Si nanotube sample is complemented with a Li foil and a Celgard 2325 separator. 1.0 M lithium hexafluorophosphate ($LiPF_6$) in 50:50 (v/v) ethylene carbonate (EC) and diethyl carbonate (DEC) was added as the electrolyte. The cell was then assembled in CR2032 coin cell cases from MTI Corporation and sealed with the MSK-160E crimper from MTI Corporation applying 1.0 Torr. The assembly was realized in an Ar glovebox from Innovative Technology. The cell was left in the Ar glovebox overnight after assembly in order to let the electrolyte diffuse in all available volume before electrochemical measurements were started. Cyclic voltammetry was conducted in the two-electrode configuration with an Interface 1000 potentiostat from Gamry Instruments, USA, at scan rates of 0.1 to 2 mV s^{-1} in the potential range from 0.005 V to 1.600 V (with respect to the lithium metal counter-electrode). Galvanostatic electrochemical impedance spectroscopy measurements (galvanostatic EIS) were completed with an amplitude of 1 µA (rms) without any DC current flow, over the frequency range of 1 mHz to 1 kHz. Samples were tested by galvanostatic EIS before and after specific numbers of charge-discharge cycles. The status of the interface of the electrode was also studied by galvanostatic EIS at various potentials in the vicinity of the CV peaks. For this, the sample was charged (or discharged) at 5 μA and stopped at the desired potential. The sample was then potentiostatically held at this potential until the measured current fell below 1 μA before galvanostatic EIS was performed. Finally, the stability of Si nanotubes as an anode material was tested at a constant current density, 7.96 µA cm^{-2} for 100 cycles. Its cyclic performance was also characterized with 10 charge / discharge cycles at different current densities between 7.96 and 79.55 µA cm^{-2}. The voltage profiles of Si nanotubes are recorded by applying a constant current of 1 μA during discharging process until the potential of the cells decreases to 0.005 V. The same current is used for charging the cells until the cells are charged up to 1.600 V. After charged with constant current, the cells are then charged with constant voltage (1.600 V) until the current drops to 0.1 μA, in order to accomplish further charging.

3. Results and discussion

3.1. Aluminothermic reduction of SiO_2 nanotubes

Industrial reduction of SiO_2 to Si element is performed at very elevated temperature (1700 °C) using carbon as the reducing agent [40]. Less extreme temperatures are rendered possible by lithium, as published earlier [39]. However, the limited vapor pressure of metallic Li forces the procedure to be performed at 700 °C, which renders the handling of large brittle samples impractical. A more practical solution is offered by the mixture of aluminum metal

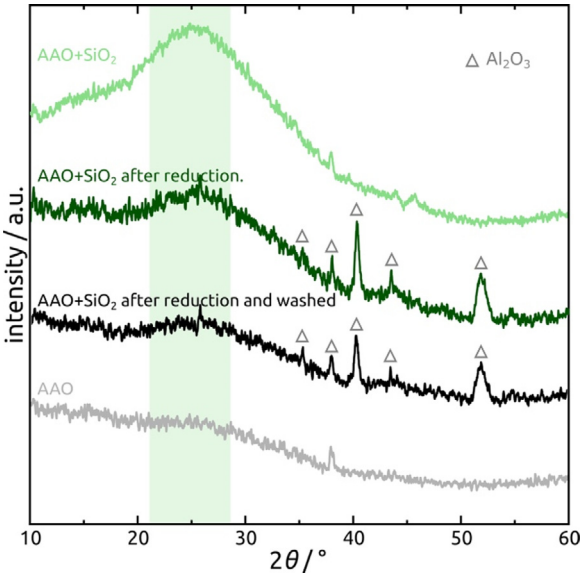

Fig. 2. X-ray diffraction patterns of pure AAO template (grey), as-deposited SiO_2 on AAO template (light green), SiO_2 sample after reduction (olive), SiO_2 samples after reduction and washed (black) (For interpretation of the references to color in this figure legend, the reader is referred to the web version of this article.).

with $AlCl_3$, applied to powdered SiO_2 at 250 °C [38] to 270 °C [41] more recently. We find that this procedure is also applicable to monolithic samples, although the larger transport distances from the Al/$AlCl_3$ mixture (present as a powder separated from the sample by a few mm) to every point of the sample necessitate the use of 400 °C to reach completion of the reaction. As illustrated in **Fig. S2**, after the aluminothermic reduction reaction, samples turn to be darker. A black color of the sample indicates a high degree of conversion from SiO_2 to Si when a mixture of 1:5 (w/w) Al and $AlCl_3$ is used. The chemical identity of the product before and after removal of the reaction by-products and excess reagents in 10 wt% H_3PO_4 is demonstrated by a combination of material characterization techniques (XRD, ATR-IR, ^{29}Si CP-MAS NMR, UV-visible absorption, SEM, EDX and Raman spectroscopy).

X-ray diffraction (Fig. 2) does not evidence the formation of any clearly crystalline phase beyond those of Al_2O_3 (JCPDS #10-0414) at $2\theta = 35.1^0$, 37.9^0, 40.2^0, 43.5^0, and 51.6^0, as marked in Fig. 2 [42]. Since the alumina template is amorphous and known to stay amorphous to temperatures of at least 1000°C, the presence of a novel crystalline alumina phase is a highly likely sign of the reduction reaction's success (with Si and Al_2O_3 as the two products). Silicon, however, is not visible – at best, the XRD pattern hints at the presence of amorphous SiO_2 with the very broad signal centered near 24^0 (before reduction, navy blue curve) [43–48], which disappears upon reduction.

More unequivocal evidence for the chemical identity of the reduced samples is delivered by a combination of spectroscopic methods, Fig. 3. The lustrous black color of the samples obtained after reduction and by-product removal (**Fig. S1**) and quantified by UV-visible absorption spectroscopy (measured in reflectance, Fig. 3**a**), qualitatively indicates the success of the reaction. ^{29}Si CP-MAS NMR analysis proves its completeness within the accuracy limits of the method, since the SiO_2 peak at −110 ppm ($Si(OSi)_4$ or "Q4" sites) [49,50] disappears fully (Fig. 3**b**). The tiny shoulders at −101 ppm and −93 ppm [49] indicate the presence of small amounts of silanol groups, ($Si(OSi)_3(OH)$ (or "Q3" sites) and ($Si(OSi)_2(OH)_2$ (or "Q2" sites), respectively. As hydroxyl-containing silica groups are overestimated in Cross Polarization spectra, the ^{29}Si CP-MAS NMR spectrum of as-deposited SiO_2 nanotubes proves a high degree of condensation of SiO_2. These conclusions are corroborated by the ATR-IR spectra shown in Fig. 3**c**. A prominent absorption band at 1073 cm^{-1} (with a shoulder at 1197 cm^{-1}) appears in the sample before reduction and reveals the existence of SiO_2, associated with the asymmetric stretching vibrations of the SiO—Si moiety in tetrahedral geometry [51,52]. Minor bands near 793 cm^{-1} and 913 cm^{-1} are assigned to the bending vibration of SiO Si [53], and some silanol groups [48,51], respectively. In our case, it should be related to Si—OH stretching vibration [52]. These peaks vanish after reduction, proving again that the conversion is complete. Only one band at 1128 cm^{-1} exists after reduction, which is related to AlO stretching mode of γ-alumina [54]. It is not detectable in the sample before reduction since it overlaps with the band at 1197 cm^{-1}.

SEM micrographs (Fig. 4**a, b**) document the morphology of Si nanotubes after reduction. Close inspection of Fig. 4**a** reveals that the pores of the AAO template are filled with excess reagents and/or by-products after reduction. After the sample has been rinsed with diethyl ether and dipped in 10 wt% H_3PO_4 at 50 °C for 3 min, the pores are open again, as shown in Fig. 4**b**, with some roughness remaining on the pore walls. This conforms with the disappearance of the Cl signal (from $AlCl_3$) in EDX after H_3PO_4 washing (from Fig. 4**c** to Fig. 4**d**).

An additional piece to the analysis puzzle is provided by Raman spectroscopy. A sapphire wafer (grey curve in Fig. 5) is used as a substrate here. The sample after reduction (olive curve in Fig.5) yields a relatively broad band centered at 481 cm^{-1} (highlighted in yellow), which reveals the existence of amorphous Si [55–57]. Other peaks, marked with squares are contributed by Al_2O_3 [58,59]. They are slightly shifted compared to the peaks from sapphire, which is due to the presence of some alumina in the sample as a by-product of the reduction reaction (in addition to the sapphire substrate). Consistent with this, these peaks are absent from the Raman spectrum of the sample with SiO_2 nanotubes in the amorphous AAO matrix [60].

Final proof for the chemical identity of as-deposited SiO_2 tubes and of the sample after aluminothermic reduction is provided by X-ray photoelectron spectroscopy (XPS): Fig. 6 presents the XPS spectra of these two samples in the Si 2p, O 1s and Al 2p regions. The corresponding survey spectra are accessible in **Fig. S3**, and they disclose the expected elements in addition to some minor contamination by the stainless steel sample holder. More interestingly, the Si 2p signal, which consists of a single SiO_2 peak after ALD, changes completely after reduction. Its very large shift in binding energy, from 103.5 eV (Si^{4+} in SiO_2) [61] to 98.6 eV (Si^0) [62–64], reveals the oxidation state change of Si to its elemental form. Of course, a layer of native oxide (102.1 eV, SiO_x) [65] is formed upon sample transfer to XPS but is sufficiently thin that the underlying amorphous Si is still clearly observable. Other elements also exhibit the transformations associated with the reduction reaction. The O 1 s spectrum before reduction shows a perfect single peak generated by the SiO_2 ALD coating (532.8 eV).[66] After reduction, the main O 1s signal is found at 531.5 eV and is associated with the Al_2O_3 generated as the by-product (in addition perhaps to the AAO matrix) [67], in addition to the small amount of SiO_2 generated by aerobic oxidation at 533.0 eV [66]. Remember that ^{29}Si NMR detects no bulk amounts of silicon oxide after reduction (Fig. 3**b**).

4. Electrochemical performance

Together, all materials characterization results presented above demonstrate unambiguously that amorphous Si nanotubes are successfully obtained. Let us now proceed to the electrochemical performance of these samples. The samples will be characterized by cyclic voltammetry, galvanostatic cycling and electrochemical

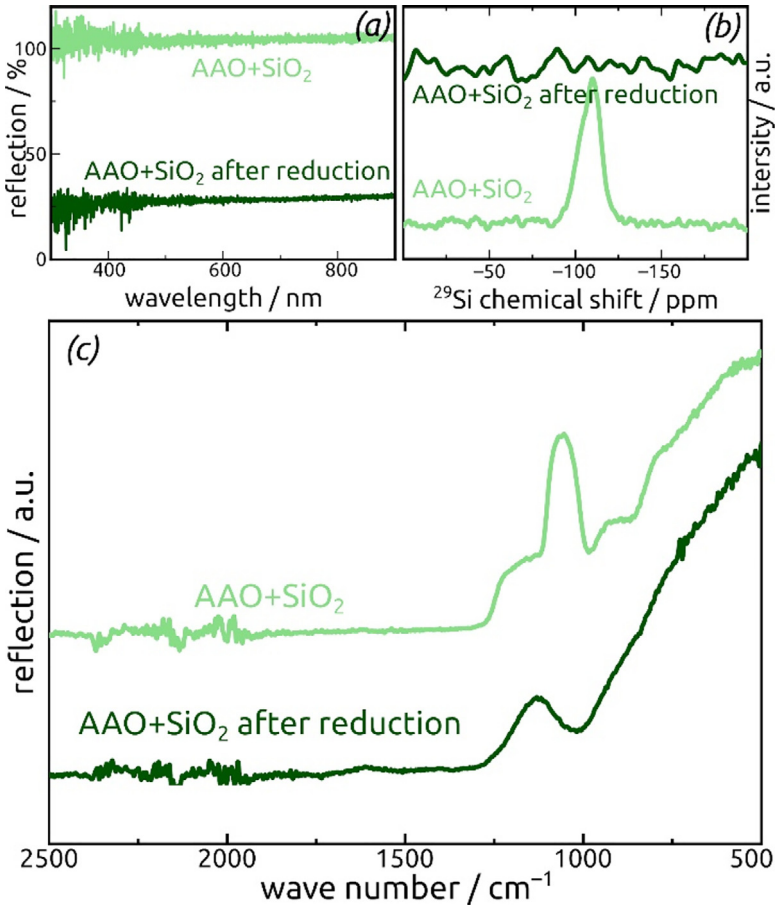

Fig. 3. Characterization of as-deposited SiO_2 nanotubes in AAO matrix (light green) and Si nanotubes (olive) obtained after reduction by *(a)* UV-visible absorption spectroscopy and *(b)* ^{29}Si CP-MAS NMR, while *(c)* shows ATR-IR spectra for these two samples (For interpretation of the references to color in this figure legend, the reader is referred to the web version of this article.).

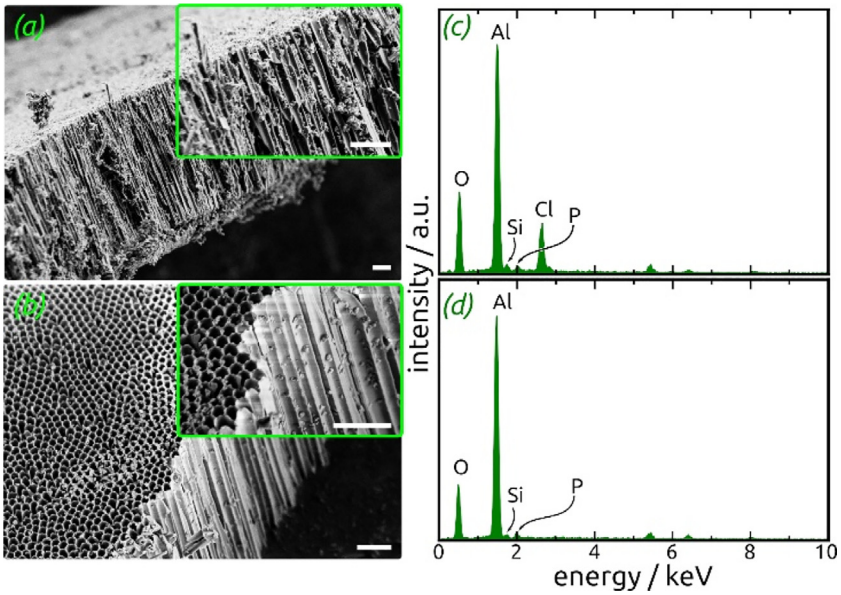

Fig. 4. SEM micrographs for cross sections of the samples *(a)* immediately after reduction and *(b)* after reduction plus washing with 10 wt% H_3PO_4. The scale bars represent 2 μm length. The element analyses of samples shown in *(a)* and *(b)* are illustrated by EDX spectra *(c)* and *(d)*, respectively.

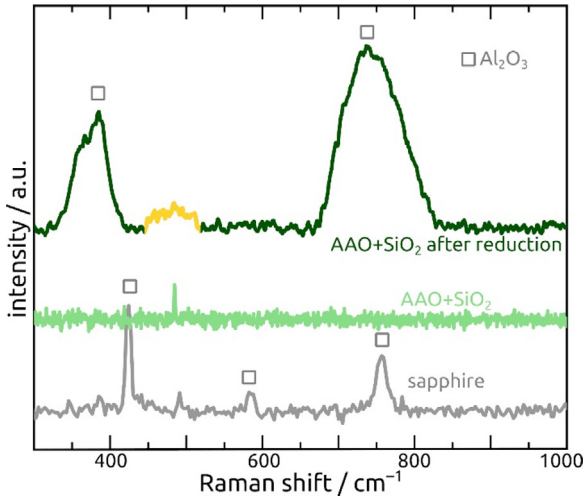

Fig. 5. Raman spectra of: sapphire serving as substrate for samples measuring Raman spectroscopy, grey; as-deposited SiO_2 nanotubes in AAO matrix, light green; Si nanotubes in AAO matrix, olive, with the peak associated with amorphous Si highlighted in yellow color (For interpretation of the references to color in this figure legend, the reader is referred to the web version of this article.).

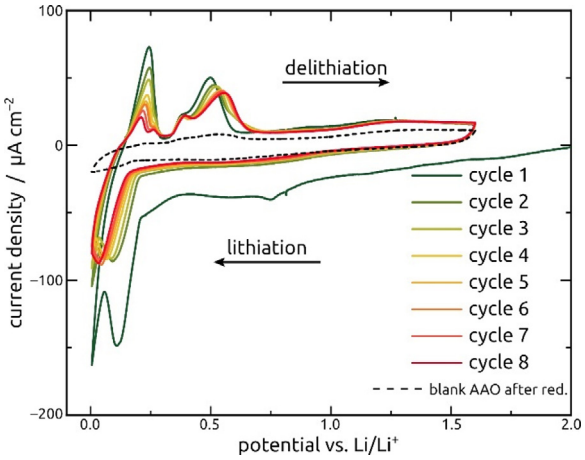

Fig. 7. Cyclic voltammograms of a Si nanotube electrode recorded at a scan rate of 0.1 mV s^{-1} in the potential range from 0.005 V to 1.600 V. A blank sample without SiO_2 ALD but otherwise submitted to all preparative steps is also measured for comparison (black dashed line).

impedance spectroscopy, with the goal of contrasting the behavior of our simplified model system with classical electrodes that consist of powders and include additives (binder, carbon). Our Si nanotube samples only need sputtering a gold layer as the electrical contact without any extra additives to be turned into functional electrodes. They are complemented with Li foil in CR2032 button cells for measurements.

Fig. 7 presents eight cyclic voltammetry cycles of our Si nanotube electrode. A blank anodic alumina sample presented for comparison behaves purely as a capacitor (dashed line). In contrast to this, the Si nanotube electrode features well-defined peaks originating from the lithiation and delithiation of a-Si. During the very first cathodic sweep, a large charge flows into the irreversible reactions associated with the formation of a solid-electrolyte interface (SEI) on the electrode surface, with a distinctive peak at 0.747 V [22,23,68]. This peak vanishes in the subsequent cycles. The main reversible lithiation peak is found at 0.1 V during the first cycle and then slightly shifts to 0.03 V–0.04 V[23] over the subsequent four cycles, where it then stays as a beautifully sharp signal [68]. This sharp shape indicates an excellent accessibility of all electroactive material from the electrolyte. The slight shift over the first few cycles is usually interpreted as an increase in the maximum lithiation stoichiometry accessible [69]. The potentials corresponding to delithiation back to amorphous Si can be noticed at 208 mV, 261 mV, 396 mV and 560 mV during anodic sweeps [23,68,70–72].

In classical silicon-based electrode materials, the presence of large amounts of carbon cause a significant portion of the electrochemical response to be purely capacitive (as opposed to the Faradaic current generated by lithiation and delithiation). Insight into the contributions of capacitive and Faradaic currents to the overall response is provided by an analysis of the scan rate dependence of the voltammograms (Fig. 8) [73–75]. Indeed, the kinetics of the associated reactions are quite distinct for both cases (capacitive current depends linearly on scan rate, whereas Faradaic reac-

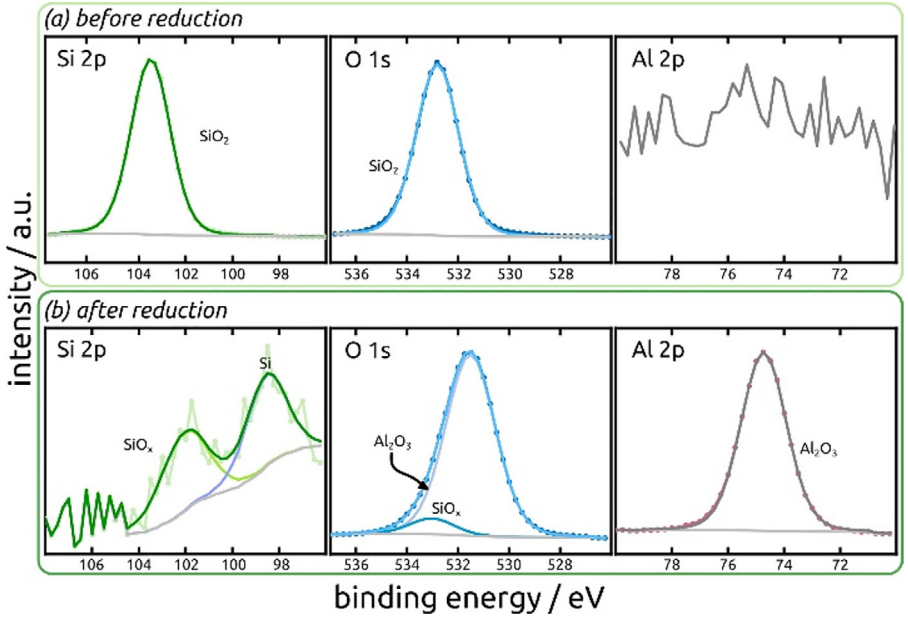

Fig. 6. X-ray photoelectron spectra of Si 2p, O 1s and Al 2p of samples *(a)* as-deposited SiO_2 with AAO matrix (before reduction) and *(b)* a reduced sample with AAO matrix.

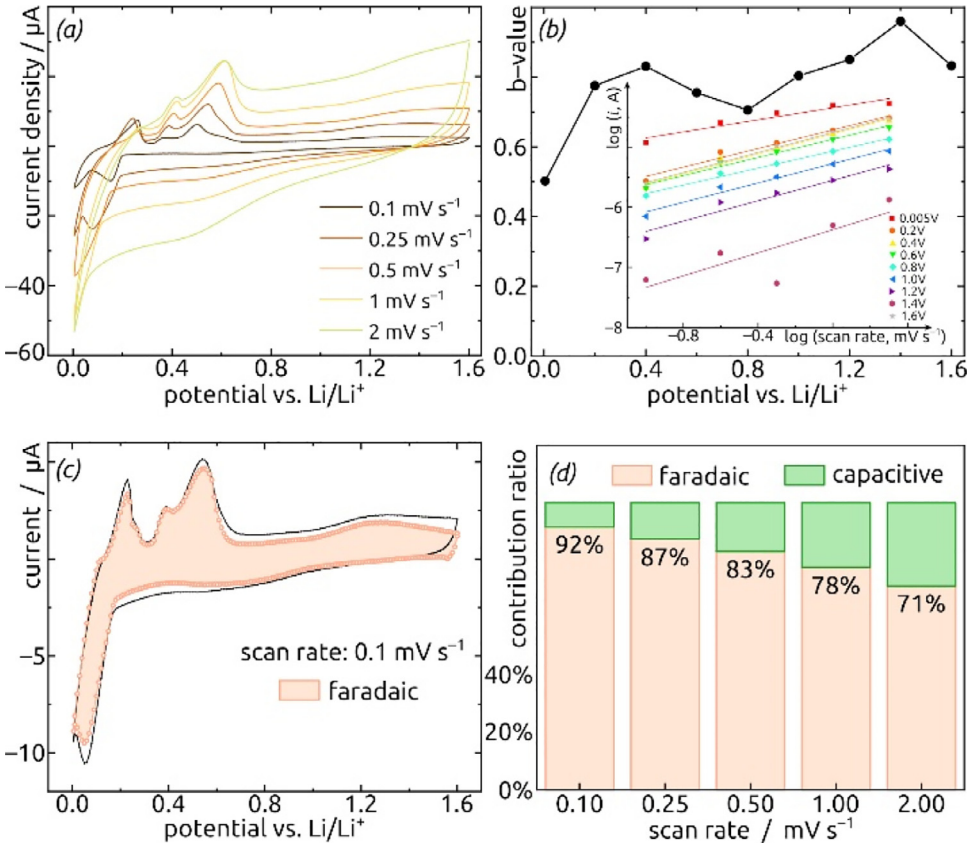

Fig. 8. *(a)* Cyclic voltammograms of Si nanotube electrode recorded at variant scan rates, υ = 0.1, 0.25, 0.5, 1, 2 mV s^{-1}. *(b)* The exponent b in the $I(\upsilon) = a\ \upsilon^b$ relationship is determined at each potential from the slope of the log-log plot (shown in the inset graph). *(c)* Faradaic contribution to the CV at 0.1 mV s^{-1}. *(d)* Integrated Faradaic contributions to CVs at different scan rates.

tions yield a square root dependence on it). In the literature, two methods have been used to separate both contributions from the experimental data.

In the first method, an empirical description of the current is expressed by Eq. (1),

$$i(V) = i_{battery} + i_{capacitance} = a\upsilon^b \tag{1}$$

or in logarithmic form,

$$\log i(V) = \log a + b \log \upsilon \tag{2}$$

Here, $i(V)$ is the current measured at a certain potential (V) at scan rate υ (mV s^{-1}). Both a and b are determined empirically from a linear fit, and b encodes the desired information [75,76]. A b value close to 0.5 represents a battery material dominated by diffusion-controlled Faradaic reactions. A b value close to 1.0 stands for a capacitive or pseudo-capacitive behavior. Fig. 8**b** shows that in our system, b strongly depends on the potential in a manner very consistent with this interpretation. At a potential close to the cathodic peak (0.005 V) we obtain $b = 0.50$ within uncertainty, indicating that all current is caused by lithiation. If the analysis is performed in potential regions remote from all peaks, b drifts to 0.96.

A second method of performing the rate dependence analysis consists in considering the current at any given potential as the sum of both contributions, Eq. (3) [73,75,77],

$$i(V) = k_1\upsilon + k_2\upsilon^{1/2} \tag{3}$$

Converting it to

$$i(V)/\upsilon^{1/2} = k_1\upsilon^{1/2} + k_2 \tag{4}$$

allows the experimentalist to extract the coefficients k_1 and k_2 from linear plots of $i(V)/v^{1/2}$ versus $v^{1/2}$. The absolute current contributions are presented for one scan rate (0.1 mV s^{-1}) in Fig. 8**c**, and after integration over the whole cycle the Faradaic contribution quantifies to an overall 92% of the electrode's total capacity. Of course, the relative contribution of Faradaic processes decreases upon increasing scan rate, yet is still 71% at 2.0 mV s^{-1} (Fig. 8**d**). These extremely large values stand in stark contrast to typical Li-ion battery electrodes, which have never exceeded the 80% mark, and have never exceeded 50% in the presence of additives [73,76,78–80]. This exceptional behavior demonstrated here establishes our Si nanotube electrode as a near-perfect model system in which the lithiation and delithiation reactions can be studied in the absence of undesired artefacts associated with the additives.

An alternative investigation of the kinetics of electrochemical reactions is provided by electrochemical impedance spectroscopy (EIS). Galvanostatic EIS measurements are presented for a pristine electrode and at 1.60 V after running 20 to 25 CV cycles over the frequency range 100 mHz–100 kHz in Fig. 9**a**. (EIS datasets recorded at various potentials are presented in the Supporting Information, **Figs. S4,S5, Table S1**.) For the pristine sample, a semicircle in the higher frequency range is complemented with a straight line at lower frequencies, which can be modeled using a simple equivalent circuit (Fig. 9**d**). After 20 cycles of CV measurements, a broader semicircle is formed, which can be interpreted as the overlap two smaller semicircles associated with impedance of charge transfer at the solid surface and across the solid electrolyte interface (SEI, Fig. 9**e**). Table 1 summarizes the values obtained from the fitted EIS data. Inspection of these values elicits several comments. First, the series resistances are high, due to the absence of the electronically conducting additive. Second, Fig. 9**b,c** reveal that the charge transfer resistance (R_{ct}) continuously increases upon cy-

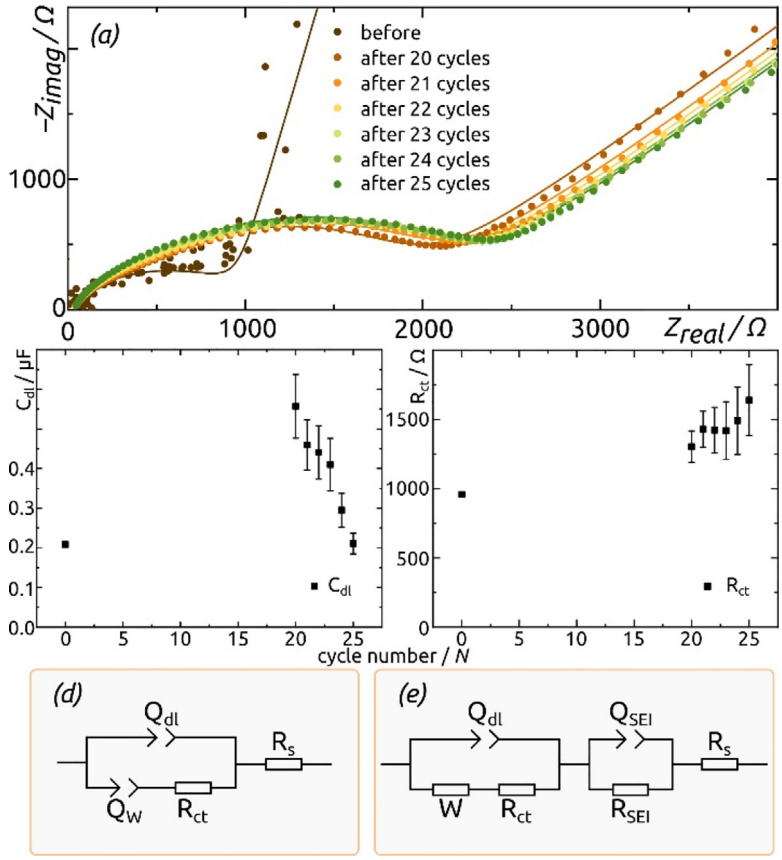

Fig. 9. *(a)* Nyquist plots of galvanostatic electrochemical impedance spectroscopy (EIS) measurements recorded of Si nanotube electrode (L = 30 µm, 4 mm macroscopic sample diameter) in their delithiated state after N CV cycles (N = 0, 20, 21, 22, 23, 24 and 25). Spectra are plotted in dots while the fitted curves are plotted as lines. *(b)* and *(c)* exhibit C_{dl} and R_{ct} values after N cycles. *(d)* demonstrates the equivalent electrical circuit model used for fitting EIS spectra before CV, while *(e)* is used for fitting EIS spectra after some CV cycles. Q_{dl}: constant-phase element due to double layer; R_{ct}: resistance of charge transfer; Q_{SEI}, R_{SEI}: constant-phase element and resistance due to solid electrolyte interface (SEI) layer; W: Warburg diffusion; R_s: series resistance.

Table 1
Parameters fitted from EIS spectra in Fig. 9 recorded after various numbers N of CV cycles (N = 0, 20, 21, 22, 23, 24 and 25). A single CPE element is used to describe diffusion for the EIS spectrum before CV: Q_w = 126 (±1) µS s^{α}; α = 0.8. Capacities are reported here for the CPE elements for the purpose of comparison and have been determined from the fitted values using a published procedure [82].

N	R_s / Ω	C_{SEI} / nF	R_{SEI} / Ω	C_{dl} / nF	R_{ct} / Ω	W/µS $s^{0.5}$
0	19.2 ± 1.1	NA	NA	208 ± 2	958 ± 14	
20	30.8 ± 1.7	54.9 ± 4.2	557 ± 92	557 ± 80	1300 ± 110	272 ± 5
21	31.7 ± 1.6	57.4 ± 4.4	580 ± 100	459 ± 64	1430 ± 130	259 ± 4
22	31.8 ± 1.6	55.9 ± 4.0	660 ± 140	441 ± 67	1420 ± 160	246 ± 4
23	32.2 ± 1.7	55.8 ± 3.8	710 ± 180	410 ± 66	1420 ± 210	239 ± 4
24	32.5 ± 1.7	62.6 ± 5.0	640 ± 220	298 ± 43	1490 ± 240	239 ± 4
25	33.0 ± 1.6	73.1 ± 7.4	530 ± 230	210 ± 26	1640 ± 260	229 ± 4

cling, whereas R_{SEI} stabilizes. These results hint at a limited stability of our electrodes.

Further insight into the often cited permanent instability of the SEI of Si electrodes [81] is provided by the comparison of equivalent circuit element values recorded not over the very first cycles but between 20th and 25th cycles. Carbon-based electrodes give rise to EIS parameters that change over the first 10 or so cycles but then tend towards stable values. Table 1 shows that instead, both R_{SEI} and R_{ct} vary from cycle to cycle in a manner that is not even monotonic. The value of R_{ct} is affected by the formation of the SEI layer since the interface changes from Si/electrolyte to Si/SEI, but this qualitative change cannot explain further variations in R_{ct} at $N \geq 20$. The fact that C_{dl} also varies hints at a non-stable geometric interface area. This could most likely be due to a roughening of the interface generated by the constant volume changes occurring upon cycling. Further changes in these values might be associated with the swelling of the SEI layer and its reorganization at every cycle, which affects the transfer of lithium ions.

All the effects highlighted by the fundamental investigative techniques shown above determine the functional performance of the cells, defined by charge-discharge curves recorded at constant current density. The voltage profiles obtained for Si nanotube electrodes under 1 μA (7.96 μA cm^{-2}) between 0.005 V and 1.600 V are presented in Fig. 10 and **Fig. S6**. The irreversible side-reactions that occur during the first cycle (Fig. 7) are visible here, as well. The plateau found around 0.2 V to 0.3 V for the first charging curve becomes weaker in the following cycles and is due to SEI layer formation. The curve shape is in line with the voltammetry shown in

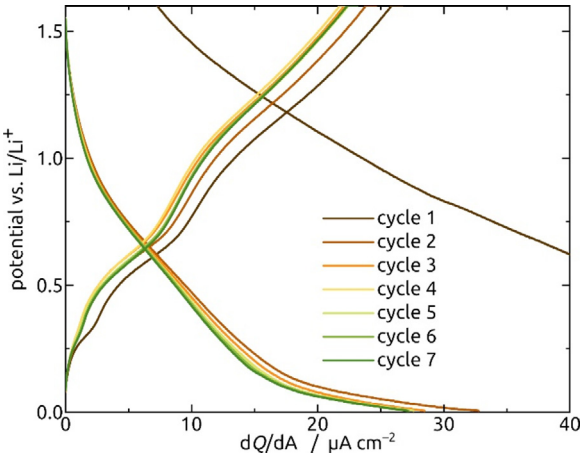

Fig. 10. Voltage profiles of Si nanotube electrode (ℓ = 40 nm, L = 30 μm, 4 mm macroscopic sample diameter) are recorded at a constant current of 1 μA. The potential window applied here is 0.005 V to 1.600 V.

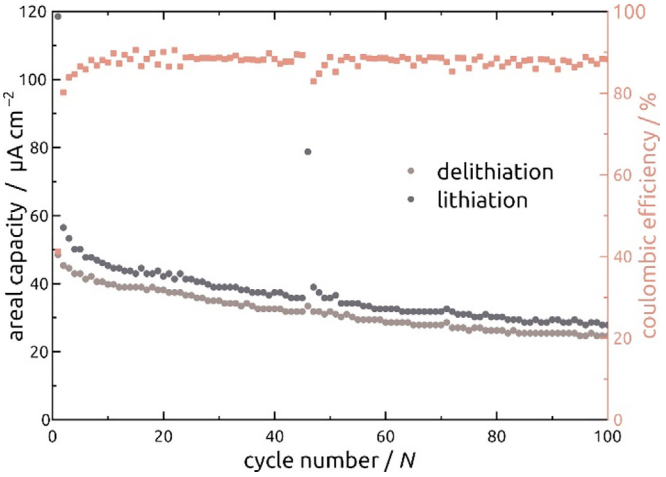

Fig. 11. The areal capacity of the Si nanotube electrode over 100 cycles at a constant current density of 7.96 μA cm^{-2}. A sub-unity Coulombic efficiency is exhibited.

Fig. 8, with slightly more prominent plateaus than typical in the Si literature, corresponding to the sharper than usual voltammetry peaks.

The stability of the electrode upon subsequent cycles is quantified over a larger number of cycles as illustrated in Fig. 11. The large capacity loss over the first cycle (Coulombic efficiency 41%) is the most significant, and the Coulombic efficiency stabilizes after approximately seven cycles, albeit not at 100%. Accordingly, the capacity continuously fades, with a retention of 51% after 100 cycles.

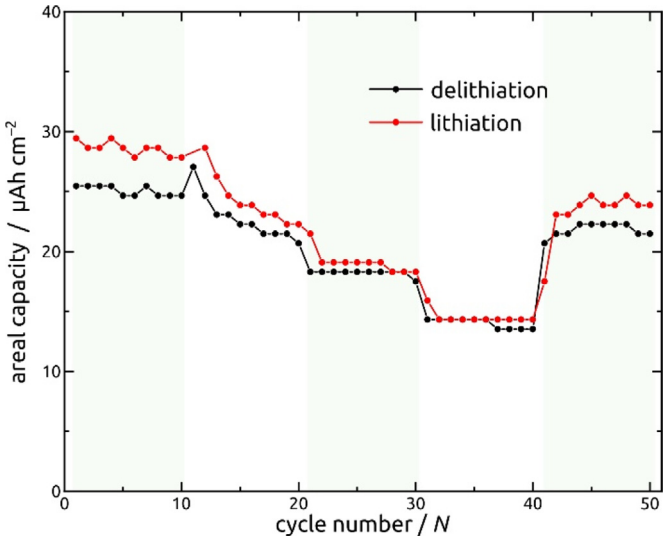

Fig. 12. Cyclic performance of the Si nanotube electrode at various current densities: 8.0, 15.9, 39.8, 79.6 and back to 8.0 μA cm^{-2}. 10 cycles of charge / discharge are recorded under each current density.

The rate performance of the Si nanotube electrode is evaluated under different current densities, Fig. 12. The data reveal that increasing the current density by a factor 10 only causes a capacity loss of 44%. This is a rather small loss for silicon [19,22,32,83], and it indicates that the very homogeneous nanotube morphology renders all electroactive material accessible to the lithium from the electrolyte. Furthermore, the capacity loss is not irreversible, indicating that no material loses electrical contact as a results of silicon's drastic volume variations.

Fig. 13 presents the analysis of a sample after electrochemical measurements. The overall morphology of the a-Si nanotubes in the AAO matrix is retained, as well as the elemental composition. The comparison with Fig. 4 indicates that the surface roughness has increased due to the volume variations upon charge and discharge. However, no pulverization is observed.

5. Conclusions and outlook

This study establishes a method for the reproducible generation of electroactive silicon nanotube samples of well-defined shape and area. The method relies on atomic layer deposition of amorphous SiO_2 nanotubes onto the inner pore walls of anodized alumina templates. The key step is the subsequent aluminothermic reduction reaction performed with a mixture of Al and $AlCl_3$ at

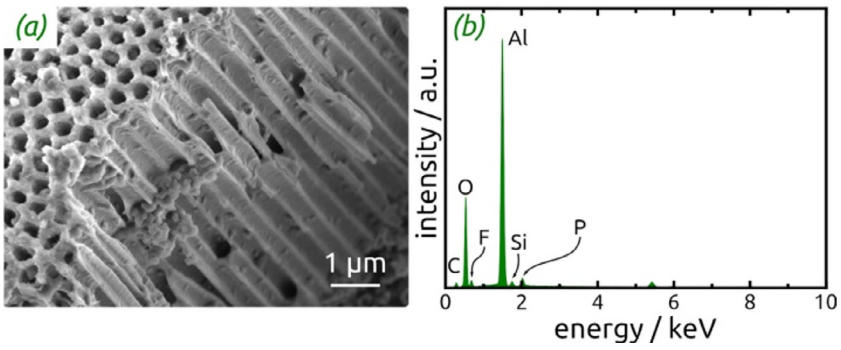

Fig. 13. *(a)* SEM micrograph and *(b)* EDX spectrum of the Si nanotube sample after stability and cyclic performance tests.

400 °C. Not only the black color of the sample obtained after reduction but also extensive characterization performed by XRD, ^{29}Si NMR, UV-visible absorption spectroscopy, ATR-IR, and XPS, prove the formation of amorphous Si in the shape of parallel, straight, vertical nanotubes embedded in an inert alumina matrix.

The electrochemical tests reveal that this material behaves as a 'pure' model system for the use of silicon as a lithium ion battery electrode material. Its poor stability is in line with the literature. However, its high rate stability and almost perfect Faradaic behavior are in stark contrast to most papers associated with silicon. The reason is the particulate nature of silicon used for those papers.

Firstly, unconnected particles necessitate the presence of additives: carbonaceous conductive material and polymeric binders contribute significant pseudocapacitive currents which complicate the analysis of results. The straight and direct contact provided to the current collector by our nanotube system circumvents the need for additives, and therefore allows for an unhindered insight into the pure material's behavior. Secondly, particles of roughly spherical shape give rise to long transport distances inside the solid, whereas the thin walls of our nanotubes enable fast charging and discharging.

Based on this well-characterized pure material, engineers can adapt it to any desired set of functional performance parameters by combining it with other electroactive materials, in particular carbon. This designer approach based on a fundamental understanding of each component differs from the trial and error method that has often prevailed.

6. Declaration of Competing Interest

There are no conflicts to declare.

Declaration of Competing Interest

The authors declare no conflict of interest.

Credit authorship contribution statement

Ying Zhuo: Investigation, Writing- original draft, Data curation, Formal analysis, Visualization. **Hong Sun:** Investigation. **Md. Helal Uddin:** Investigation. **Maïssa K.S. Barr:** Investigation. **Dorothea Wisser:** Investigation, Writing- original draft. **Philip Roßmann:** Investigation. **Julian D. Esper:** Investigation. **Sarah Tymek:** Investigation, Visualization. **Dirk Döhler:** Investigation, Visualization. **Wolfgang Peukert:** Resources. **Martin Hartmann:** Resources. **Julien Bachmann:** Conceptualization, Resources, Writing- review & editing, Supervision, Project administration, Data curation, Funding acquisition.

Acknowledgements

This work was financed by the European Research Council via the ERC Consolidator Grant 'Solacylin' (grant agreement 647281).

Supplementary materials

Supplementary material associated with this article can be found, in the online version, at doi:10.1016/j.electacta.2021.138522.

References

[1] G.M. Joselin Herbert, S. Iniyan, E. Sreevalsan, S. Rajapandian, A review of wind energy technologies, Renew. Sust. Energ. Rev. 11 (2007) 1117–1145.
[2] R. Billinton, G. Bai, Generating capacity adequacy associated with wind energy, IEEE Trans. Energy Convers. 19 (2004) 641–646.
[3] T. Ackermann, L. Söder, An overview of wind energy-status 2002, Renew. Sust. Energ. Rev. 6 (2002) 67–128.
[4] M.M. Lee, J. Teuscher, T. Miyasaka, T. Murakami, H.J. Snaith, Efficient hybrid solar cells based on meso-superstructured organometal halide perovskites, Science 338 (2012) 643–647.
[5] N.S. Lewis, D.G. Nocera, Powering the planet: Chemical challenges in solar energy utilization, PNAS USA 103 (2006) 15729–15735.
[6] B. O'regan, M. Grätzel, A low-cost, high-efficiency solar cell based on dye-sensitized colloidal TiO_2 films, Nature 353 (1991) 737–740.
[7] X. Chen, W. He, L. Ding, S. Wang, H. Wang, Enhancing interfacial contact in all solid state batteries with a cathode-supported solid electrolyte membrane framework, Energy Environ. Sci. 12 (2019) 938–944.
[8] S. Goriparti, E. Miele, F. De Angelis, E. Di Fabrizio, R.P. Zaccaria, C. Capiglia, Review on recent progress of nanostructured anode materials for Li-ion batteries, J. Power Sources 257 (2014) 421–443.
[9] R. Yi, F. Dai, M.L. Gordin, S. Chen, D. Wang, Micro-sized Si-C composite with interconnected nanoscale building blocks as high-performance anodes for practical application in lithium-ion batteries, Adv. Energy Mater. 3 (2013) 295–300.
[10] D. Liu, Z. Liu, X. Li, W. Xie, Q. Wang, Q. Liu, Y. Fu, D. He, Group IVA element (Si, Ge, Sn)-based alloying/dealloying anodes as negative electrodes for full-cell lithium-ion batteries, Small 13 (2017) 1702000.
[11] J. Li, S. Hwang, F. Guo, S. Li, Z. Chen, R. Kou, K. Sun, C.-J. Sun, H. Gan, A. Yu, E.A. Stach, H. Zhou, D. Su, Phase evolution of conversion-type electrode for lithium ion batteries, Nat. Commun. 10 (2019) 2224.
[12] N. Nitta, F. Wu, J.T. Lee, G. Yushin, Li-ion battery materials: present and furture, Mater. Today 18 (2015) 252–264.
[13] X. Su, Q. Wu, J. Li, X. Xiao, A. Lott, W. Lu, B.W. Sheldon, J. Wu, Silicon-based nanomaterials for lithium-ion batteries: a review, Adv. Energy Mater. 4 (2014) 1300882.
[14] Y. Han, G. Huang, S. Xu, Structural reorganization-based nanomaterials as anodes for lithium-ion batteries: design, preparation, and performance, Small 16 (2020) e1902841.
[15] U. Kasavajjula, C. Wang, A.J. Appleby, Nano- and bulk-silicon-based insertion anodes for lithium-ion secondary cells, J. Power Sources 163 (2007) 1003–1039.
[16] W.U. Rehman, H. Wang, R.Z.A. Manj, W. Luo, J. Yang, When silicon materials meet natural sources: opportunities and challenges for low-cost lithium-storage, Small (2019) 1904508.
[17] Y. An, Y. Tian, H. Wei, B. Xi, S. Xiong, J. Feng, Y. Qian, Porosity- and graphitization-controlled fabrication of nanoporous silicon@carbon for lithium storage and its conjugation with MXene for lithium-metal anode, Adv. Funct. Mater. 30 (2019) 1908721.
[18] M.N. Obrovac, V.L. Chevrier, Alloy negative electrodes for Li-ion batteries, Chem. Rev. 114 (2014) 11444–11502.
[19] J. Ahn, B. Kim, G. Jang, J. Moon, Magnesiothermic reduction-enabled synthesis of Si-Ge alloy nanoparticles with canyon-like surface structure for Li-ion battery, ChemElectroChem 5 (2018) 2729–2733.
[20] C.-M. Park, J.-H. Kim, H. Kim, H.-J. Sohn, Li-alloy based anode materials for Li secondary batteries, Chem. Soc. Rev. 39 (2010) 3115–3141.
[21] H. Kim, M. Seo, M.-H. Park, J. Cho, A critical size of silicon nano-anodes for lithium rechargeable batteries, Angew. Chem. Int. Ed. 49 (2010) 2146-2149.; Angew. Chem. 122 (2010) 2192-2195.
[22] X. Zhou, L.-J. Wan, Y.-G. Guo, Electrospun silicon nanoparticle/porous carbon hybrid nanofibers for lithum-ion batteries, Small 9 (2013) 2684–2688.
[23] W.-J. Yu, C. Liu, P.-X. Hou, L. Zhang, X.-Y. Shan, F. Li, H.-M. Cheng, Lithiation of silicon nanoparticles confined in carbon nanotubes, ACS Nano 9 (2015) 5063–5071.
[24] T.M. Higgins, S.-H. Park, P.J. King, C. Zhang, N. McEvoy, N.C. Berner, D. Daly, A. Shmeliov, U. Khan, G. Duesberg, V. Nicolosi, J.N. Coleman, A commercial conducting polymer as both binder and conductive additive for silicon nanoparticle-based lithium-ion battery negative electrodes, ACS Nano 10 (2016) 3702–3713.
[25] L.-F. Cui, R. Ruffo, C.K. Chan, H. Peng, Y. Cui, Crystalline-amorphous core-shell silicon nanowires for high capacity and high current battery electrodes, Nano Lett 9 (2009) 491–495.
[26] C.K. Chan, H. Peng, G. Liu, K. Mcllwrath, X.F. Zhang, R.A. Huggins, Y. Cui, High--performance lithium battery anodes using silicon nanowires, Nat. Nanotechnol. 3 (2008) 31–35.
[27] C. Yue, Y. Yu, Z. Wu, X. He, J. Wang, J. Li, C. Li, S. Wu, J. Li, J. Kang, Enhanced reversible lithium storage in germanium nano-island coated 3D hexagonal bottle-like Si nanorod arrays, Nanoscale 6 (2014) 1817–1822.
[28] M.-H. Park, M.G. Kim, J. Joo, K. Kim, J. Kim, S. Ahn, Y. Cui, J. Cho, Silicon nanotube battery anodes, Nano Lett 9 (2009) 3844–3847.
[29] B.D. Polat, O. Keles, Functionally graded Si based thin films as negative electrodes for next generation lithium ion batteries, Electrochim. Acta 187 (2016) 293–299.
[30] D. Cho, M. Kim, J. Hwang, J.H. Park, Y.L. Joo, Y. Jeong, Facile synthesis of porous silicon nanofibers by magnesium reduction for application in lithium ion batteries, Nanoscale Res. Lett. 10 (2015) 424.
[31] G. Hwang, H. Park, T. Bok, S. Choi, S. Lee, I. Hwang, N.-S. Choi, K. Seo, S. Park, A high-performance nanoporous Si/Al_2O_3 foam lithium-ion battery anode fabricated by selective chemical etching of the Al-Si alloy and subsequent thermal oxidation, Chem. Commun. (Camb) 51 (2015) 4429–4432.
[32] F.-H. Du, B. Li, W. Fu, Y.-J. Xiong, K.-X. Wang, J.-S. Chen, Surface binding of polypyrrole on porous silicon hollow nanoshperes for Li-ion battery anodes with high structure stability, Adv. Mater. 26 (2014) 6145–6150.

[33] Y. He, X. Yu, Y. Wang, H. Li, X. Huang, Alumina-coated patterned amorphous silicon as the anode for a lithium-ion battery with high coulombic efficiency, Adv. Mater. 23 (2011) 4938–4941.
[34] S. Bourderau, T. Brousse, D.M. Schleich, Amorphous silicon as a possible anode material for Li-ion batteries, J. Power Sources 81-82 (1999) 233–236.
[35] L. Zhao, D.J. Dvorak, M.N. Obrovac, Layered amorphous silicon as negative electrodes in lithium-ion batteries, J. Power Sources 332 (2016) 290–298.
[36] J.R. Szczech, S. Jin, Nanostructured silicon for high capacity lithium battery anodes, Energy Environ. Sci. 4 (2011) 56–72.
[37] B. Liang, Y. Liu, Y. Xu, Silicon-based materials as high capacity anodes for next generation lithium ion batteries, J. Power Sources 267 (2014) 469–490.
[38] Y. Zhuo, S. Tymek, H. Sun, M.K.S. Barr, L. Santinacci, J. Bachmann, Ordered SnO_2 nanotube arrays of tuneable geometry as a lithium ion battery material with high longevity, Nanoscale Adv 2 (2020) 1417–1426.
[39] T. Grünzel, Y.J. Lee, K. Kuepper, J. Bachmann, Preparation of electrochemically active silicon nanotubes in highly ordered arrays, Beilstein J. Nanotechnol. 4 (2013) 655–664.
[40] N. Lin, Y. Han, J. Zhou, K. Zhang, T. Xu, Y. Zhu, Y. Qian, A low temperature molten salt process for aluminothermic reduction of silicon oxides to crystalline Si for Li-ion batteries, Energy Environ. Sci. 8 (2015) 3187–3191.
[41] Z.-W. Zhou, Y.-T. Liu, X.-M. Xie, X.-Y. Ye, Aluminothermic reduction enabled synthesis of silicon hollow microspheres from commercialized silica nanoparticles for superior lithium storage, Chem. Commun. (Camb) 52 (2016) 8401–8404.
[42] C. Tian, H. Lin, D. Zhang, P. Zhang, R. Hong, Z. Han, X. Qian, J. Zou, Mn^{4+} activated Al_2O_3 red-emitting ceramic phosphor with excellent thermal conductivity, Opt. Express 27 (2019) 32666–32678.
[43] Q. Shabir, A. Pokale, A. Loni, D.R. Johnson, L.T. Canham, R. Fenollosa, M. Tymczenko, I. Rodríguez, F. Meseguer, A. Cros, A. Cantarero, Medically biodegradable hydrogenated amorphous silicon microspheres, Silicon 3 (2011) 173–176.
[44] Y. Xu, Y. Zhou, W. Ma, S. Wang, A fluorescent sensor for zinc detection and removal based on core-shell functionalized Fe_3O_4@SiO_2 nanoparticles, J. Nanomater. (2013) 1–7.
[45] J. Sun, Z. Xu, W. Li, X. Shen, Effect of nano-SiO_2 on the early hydration of alite–sulphoaluminate cement, Nanomaterials (Basel) 7 (2017) 102.
[46] Y. Liang, J. Ouyang, H. Wang, W. Wang, P. Chui, K. Sun, Synthesis and characterization of core-shell structured SiO2@YVO_4:Yb^{3+}, Er^{3+} microspheres, Appl. Surf. Sci. 258 (2012) 3689–3694.
[47] X. Wu, Z.-Q. Shi, C.-Y. Wang, J. Jin, Nanostructured SiO_2/C composites prepared via electrospinning and their electrochemical properties for lithium ion batteries, J. Electroanal. Chem. 746 (2015) 62–67.
[48] S. Musić, N. Filipović-Vinceković, L. Sekovanić, Precipitation of amorphous SiO_2 particles and their properties, Braz. J. Chem. Eng. 28 (2011) 89–94.
[49] K.-Y. Hsieh, E.-E. Bendeif, A. Gansmuller, S. Pillet, T. Woike, D. Schaniel, Structure and dynamics of guest molecules confined in a mesoporous silica matrix: complementary NMR and PDF characterization, RSC Adv 3 (2013) 26132–26141.
[50] R.A. Faulkner, J.A. DiVerdi, Y. Yang, T. Kobayashi, G.E. Maciel, The surface of nanoparticle silicon as studied by solid-state NMR, Materials 6 (2012) 18–46.
[51] H. Schumacher, U. Künzelmann, B. Vasilev, K.-J. Eichhorn, J. Bartha, Applications of microstructured silicon wafers as internal reflection elements in attenuated total reflection Fourier transform infrared spectroscopy, Appl. Spectrosc. 64 (2010) 1022–1027.
[52] Q. Zhang, C. Chen, M. Wang, J. Cai, J. Xu, C. Xia, Facile preparation of highly-dispersed cobalt-silicon mixed oxide nanosphere and its catalytic application in cyclohexane selective oxidation, Nanoscale Res. Lett. 6 (2011) 586.
[53] P. Seeharaj, P. Pasupong, E. Detsri, P. Damrongsak, Superhydrophobilization of SiO_2 surface with two alkylsilanes for an application in oil/water separation, J. Mater. Sci. 53 (2018) 4828–4839.
[54] R.R. Toledo, V.R. Santoyo, D.M. Sánchez, M.M. Rosales, Effect of aluminum precursor on physicochemical properties of Al_2O_3 by hydrolysis/precipitation method, Nova scientia 10 (2018) 83–99.
[55] S. Sorieul, J.-M. Costantini, L. Gosmain, L. Thomé, J.-J. Grob, Raman spectroscopy study of heavy-ion-irradiated α-SiC, J. Phys. Condens. Matter 18 (2006) 5235–5251.
[56] K.O. Bugaev, A.A. Zelenina, V.A. Volodin, Vibrational spectroscopy of chemical species in silicon and silicon-rich nitride thin films, Int. J. Spectrosc. (2012) 1–5.
[57] M. Ehbrecht, H. Ferkel, F. Huisken, L. Holz, Yu.N. Polivanov, V.V. Smirnov, O.M. Stelmakh, R. Schmidt, Deposition and analysis of silicon clusters generated by laser-induced gas phase reaction, J. Appl. Phys. 78 (1995) 5302–5306.
[58] I. Lorite, J.J. Romero, J.F. Fernández, Effects of the agglomeration state on the Raman properties of Co_3O_4 nanoparticles, J. Raman Spectrosc. 43 (2012) 1443–1448.
[59] K.S. Wan, S. Tochino, W.L. Zhu, S. Ohtsuka, G. Pezzotti, Quantitative evaluation of probe response functions for Raman and fluorescence bands of single-crystalline and polycrystalline Al_2O_3, J. Phys. D: Appl. Phys. 43 (2010) 205501.
[60] S. Kumari, A. Khare, Optical and structural characterization of pulsed laser deposited ruby thin films for temperature sensing application, Appl. Surf. Sci. 265 (2013) 180–186.
[61] P. Mazzoldi, A. Carnera, F. Caccavale, M.L. Favaro, A. Boscolo-Boscoletto, G. Granozzi, R. Bertoncello, G. Battaglin, N and Ar ion-implantatin effects in SiO_2 films on Si single-crystal substrates, J. Appl. Phys. 70 (1991) 3528–3536.
[62] G.E. Franklin, D.H. Rich, H. Hong, T. Miller, T.-C. Chiang, Interface formation and growth of InSb on Si(100), Phys. Rev. B Condens. Matter. 45 (1992) 3426–3434.
[63] F. Sirotti, M. De Santis, G. Rossi, Synchroton-radiation photoemission and x-ray absorption of Fe silicides, Phys. Rev. B Condens. Matter. 48 (1993) 8299–8306.
[64] A. Tabata, S. Fujii, Y. Suzuoki, T. Mizutani, M. leda, X-ray photoelectron spectroscopy (XPS) of hydrogenated amorphous silicon carbide (a-Si_xC_{1-x}:H) prepared by the plasma CVD method, J. Phys. D Appl. Phys. 23 (1990) 316–320.
[65] M. Anwar, C.A. Hogarth, R. Bulpett, An XPS study of amorphous MoO_3/SiO films deposited by co-evaporation, J. Mater. Sci. 25 (1990) 1784–1788.
[66] J. Finster, SiO_2 in 6:3 (Stishovite) and 4:2 co-ordination — characterization by core level spectroscopy (XPS/XAES), Surf. Interface Anal. 12 (1998) 309–314.
[67] D. Leinen, G. Lassaletta, A. Fernández, A. Caballero, A.R. González-Elipe, J.M. Martín, B. Vacher, Ion beam induced chemical vapor deposition procedure for the preparation of oxide thin films. II. Preparation and characterization of $Al_xTi_yO_z$ thin films, J. Vac. Sci. Technol. A 14 (1996) 2842–2848.
[68] W. Chen, Z. Fan, A. Dhanabalan, C. Chen, C. Wang, Mesoporous silicon anodes prepared by magnesiothermic reduction for lithium ion batteries, J. Electrochem. Soc. 158 (2011) A1055–A1059.
[69] H. Wu, Y. Cui, Designing nanostructured Si anodes for high energy lithium ion batteries, Nano Today 7 (2012) 414–429.
[70] Z.-W. Zhou, Y.-T. Liu, X.-M. Xie, X.-Y. Ye, Constructing novel Si@SnO_2 core-shell heterostructures by facile self-assembly of SnO_2 nanowires on silicon hollow nanospheres for large, reversible lithium storage, ACS Appl. Mater. Interfaces 8 (2016) 7092–7100.
[71] A. Magasinski, P. Dixon, B. Hertzberg, A. Kvit, J. Ayala, G. Yushin, High-performance lithium-ion anodes using a hierarchical bottom-up approach, Nat. Mater. 9 (2010) 353–358.
[72] Y. Yao, M.T. McDowell, I. Ryu, H. Wu, N. Liu, L. Hu, W.D. Nix, Y. Cui, Interconnected silicon hollow nanospheres for lithium-ion battery anodes with long cycle life, Nano Lett 11 (2011) 2949–2954.
[73] W. Tian, H. Hu, Y. Wang, P. Li, J. Liu, J. Liu, X. Wang, X. Xu, Z. Li, Q. Zhao, H. Ning, W. Wu, M. Wu, Metal-organic frameworks mediated synthesis of one-dimensional molybdenum-based /carbon composites for enhanced lithium storage, ACS Nano 12 (2018) 1990–2000.
[74] J.D. Esper, Y. Zhuo, M.K.S. Barr, T. Yokosawa, E. Spiecker, D. de Ligny, J. Bachmann, W. Peukert, S. Romeis, Shape-anisotropic cobalt-germanium-borate glass flakes as novel Li-ion battery anodes, Powder Technol 363 (2020) 218–231.
[75] J. Liu, J. Wang, C. Xu, H. Jiang, C. Li, L. Zhang, J. Lin, Z.X. Shen, Advanced energy storage devices: basic principles, analytical methods, and rational materials design, Adv. Sci. 5 (2018) 1700322.
[76] J. Li, H. Wang, W. Wei, L. Meng, Advanced MoS_2 and graphene heterostructures as high-performance anode for sodium-ion batteries, Nanotechnology 30 (2019) 104003.
[77] M. Feng, Q. Du, L. Su, G. Zhang, G. Wang, Z. Ma, W. Gao, X. Qin, G. Shao, Manganese oxide electrode with excellent electrochemical performance for sodium ion batteries by pre-intercalation of K and Na ions, Sci. Rep. 7 (2017) 2219.
[78] L. Luo, J. Song, L. Song, H. Zhang, Y. Bi, L. Liu, L. Yin, F. Wang, G. Wang, Flexible conductive anodes based on 3D hierarchical Sn/NS-CNFs@rGO network for sodium-ion batteries, Nano-Micro Lett 11 (2019) 63.
[79] J. Xiong, Q. Pan, F. Zheng, X. Xiong, C. Yang, D. Hu, C. Huang, N/S co-doped carbon derived from cotton as high performance anode materials for lithium ion batteries, Front. Chem. 6 (2018) 78.
[80] L. Zhang, X. Zhang, G. Tian, Q. Zhang, M. Knapp, H. Ehrenberg, G. Chen, Z. Shen, G. Yang, L. Gu, F. Du, Lithium lanthanum titanate perovskite as an anode for lithium ion batteries, Nat. Commun. 11 (2020) 3490.
[81] T.H. Hwang, Y.M. Lee, B.-S. Kong, J.-S. Seo, J.W. Choi, Electrospun core-shell fibers for robust silicon nanoparticle-based lithium ion battery anodes, Nano Lett 12 (2012) 802–807.
[82] B. Hirschorn, M.E. Orazem, B. Tribollet, V. Vivier, I. Frateur, M. Musiani, Determination of effective capacitance and film thickness from constant-phase-element parameters, Electrochim. Acta 55 (2010) 6218–6227.
[83] S.-C. Hou, Y.-F. Su, C.-C. Chang, C.-W. Hu, T.-Y. Chen, S.-M. Yang, J.-L. Huang, The synergistic effects of combining the high energy mechanical milling and wet milling on Si negative electrode materials for lithium ion battery, J. Power Sources 349 (2017) 111–120.